8-node hexahedral unsymmetric element with rotation DOFs for modified couple stress elasticity

Yan Shang[1, *], Chen-Feng Li[2], Kang-Yu Jia[3]

[1]*State Key Laboratory of Mechanics and Control of Mechanical Structures, College of Aerospace Engineering, Nanjing University of Aeronautics and Astronautics, Nanjing 210016, China*

[2]*Zienkiewicz Centre for Computational Engineering and Energy Safety Research Institute, College of Engineering, Swansea University, Swansea SA1 8EN, UK*

[3]*Hubei Key Laboratory of Advanced Textile Materials & Application, Wuhan Textile University, Wuhan 430200, China*

SUMMARY

A new C^0 8-node 48-DOF hexahedral element is developed for analysis of size-dependent problems in the context of the modified couple stress theory by extending the methodology proposed in our recent work [1] to the three-dimensional (3D) cases. There are two major innovations in the present formulation. First, the independent nodal rotation degrees of freedom (DOFs) are employed to enhance the standard 3D isoparametric interpolation for obtaining the displacement and strain test functions, as well as to approximatively design the physical rotation field for deriving the curvature test function. Second, the equilibrium stress functions instead of the analytical functions are used to formulate the stress trial function whilst the couple stress trial function is directly obtained from the curvature test function by using the constitutive relationship. Besides, the penalty function is introduced into the virtual work principle for enforcing the C^1 continuity condition in weak sense. Several benchmark examples are examined and the numerical results demonstrate that the element can simulate the size-dependent mechanical behaviors well, exhibiting satisfactory accuracy and low susceptibility to mesh distortion.

KEY WORDS: modified couple stress theory; size-dependent; unsymmetric FEM; hexahedral element; rotation degree of freedom

1. Introduction

Many experimental observations have shown that the micro/nano structures, which have been

∗Correspondence to: Dr. Yan Shang, State Key Laboratory of Mechanics and Control of Mechanical Structures, College of Aerospace Engineering, Nanjing University of Aeronautics and Astronautics, Nanjing 210016, China
E-mail: shangyan@nuaa.edu.cn

widely used in modern engineering applications, may experience size-dependent mechanical behaviors. Various non-classical higher-order continuum theories, such as the strain gradient theory (SGT) and the couple stress theory (CST), have been developed for describing such size-dependent phenomena [2-8]. However, as these higher-order theories are more complex than the classical one, the analytical or semi-analytical solutions are available only for restricted problems with simple geometries and certain boundary conditions. Therefore, the numerical approaches with high accuracy and efficiency are clearly required for the solution procedure, in which the well-accepted finite element method (FEM) is usually recognized as a very efficient choice. In recent year, the isogeometric method [9-12] and the meshless method [13, 14], that can formulate highly continuous basis functions, have also been applied to the size-dependent problems. However, the computation expenses of these methods are significantly larger than the FEM. Moreover, the enforcements of the boundary conditions in these methods are not as straightforward as the FEM.

In past decades, great efforts have been made to develop robust plane elements for higher-order continuum theories. For instance, Zervos et al. [15, 16] formulated different C^1 triangular and quadrilateral elements for elastoplasticity strain gradient problems; Beheshti [17] developed 4-node quadrilateral elements based on the Hermite shape functions for the strain-gradient elasticity; Papanicolopulos et al. [18] proposed a general framework for developing mixed finite elements for strain-gradient boundary-value problems using either Lagrange multiplier or penalty methods; Choi and Lee [19] extended the smoothed FEM to the modified couple stress theory; Kwon and Lee [20] proposed a mixed element formulation using the Lagrange multiplier method and the convergence criteria; Garg and Han [21, 22] developed penalty plane and axisymmetric elements for the couple stress elasticity in which the independent nodal drilling DOFs are introduced; Wang et al. [23] developed the quasi-conforming $C^{0\text{-}1}$ elements in which both nodal displacements and nodal displacement derivatives are adopted as DOFs for the modified couple stress theory; Chen and his coauthors [24, 25] also proposed similar models for the strain gradient/couple stress theories using the refined nonconforming element technique; Phunpeng and Baiz [26] constructed a mixed element for strain-gradient elasticity problems using the FEniCS environment; Sze and Wu [27] formulated three 4-node 24-DOF quadrilateral elements for the gradient elasticity analysis by generalizing different thin plate element models.

Besides, the developments of structural beam/plate elements based on size-dependent continuum

theories have also received a considerable attention from scholars. For example, Kahrobaiyan et al. [28, 29] developed Timoshenko beam elements and applied them to the MEMS; Ansari et al. [30] constructed Euler-Bernoulli and Timoshenko beam elements based on Mindlin's strain gradient theory; Reddy et al. [31] performed the nonlinear finite element analysis of the functionally graded circular plates with the modified couple stress theory; Ansari et al. [32, 33] proposed Mindlin plate elements based on the most general form of the strain gradient theory.

Compared with plane and structural elements, three-dimensional (3D) solid element models may be more important in practical engineering problems. But unfortunately, only a very limited number of 3D elements based on size-dependent continuum theories are available. In particular, no C^0 low-order 3D elements have been proposed for the modified couple stress theory. Among the existing works, Papanicolopulos et al. [34] constructed a strict C^1 hexahedral element by using the Hermite interpolations. However, this element was reported to require the usage of structured meshes. Zervos [35] presented a general finite element discretization of Mindlin's elasticity with microstructure, in which the micro and macro deformations were considered as independent variables and their relationship was constrained by an additional material parameter. Torabi et al. [36] developed a 4-node non-conforming tetrahedral element for the strain gradient elasticity, in which both the nodal displacements and their first-order derivatives were employed as the element DOFs. Zybell et al. [37] formulated a hexahedral element with 162 DOFs that was unpractical for engineering applications. Based on the mixed formulation and the convergence criteria proposed in [20], Kwon and Lee [38] also developed hexahedral elements with rotation DOFs and Lagrange multiplier DOFs, in that an additional constraint about the deviatoric curvature was also considered.

As discussed above, the FEM indeed proposes a promising approach for solving size-dependent problems. However, it is well known that the performance of the usual FEM is quite susceptible to mesh distortions that may lead to great losses of numerical accuracies, in worst cases, even the breakdown of calculations. In fact, how to develop distortion-insensitive element models has always remained as an important and open topic. Besides, another great challenge for developing robust elements based on size-dependent higher-order continuum theories with good performance and simple formulation is that a straightforward displacement-based finite element implementation of these higher-order theories would require the C^1 continuity over the element boundaries. This requirement may make the element construction procedure quite tedious.

In the recent work [1], a novel quadrilateral membrane element with four nodes and twelve DOFs has been developed in the context of the modified couple stress elasticity by using the unsymmetric FEM [39-43]. Numerical tests show that this membrane element which satisfy the weak C^1 continuity condition possesses good accuracy and distortion tolerance when analyzing the size-dependent plain strain problems.

In this paper, a new C^0 low-order 8-node 48-DOF hexahedral element is developed by extending the methodology proposed in [1] to the 3D cases. It should be noted that it is not a trivial job, and there are two major difficulties. First, it is well known that the commonly used 8-node 3D isoparametric interpolation only experiences unsatisfactory performance, especially in bending-dominated problems. In the 2D element formulation [1], the famous Allman's interpolation is used to determine the displacement test function. For the 3D cases, there are also some interpolations equipped with rotation DOFs, such as [44-46]. However, these interpolations seem somewhat complex. In this work, we propose a new 3D interpolation of such kind by directly extending the 2D formulation in [1] to the 3D case. It has more concise expressions and can coincide with the Allman's interpolation along the element boundaries. Second, the stress trial function in the 2D case [1] is constructed based on the well-known Airy stress solutions. However, the derivations of such analytical stress solutions in 3D elasticity are very tedious, which is unpractical for the FE implementation. To circumvent this obstacle, we employ the equilibrium stress functions instead of the analytical solutions to determine the stress trial function. Moreover, the couple stress trial function in this work is directly obtained from the curvature test function by using the constitutive relationship, which is also different with the 2D case. As a benefit, the new 3D element can also be applied to the classical elastic problems by simply setting the material length scale parameter as zero. Note that the 2D element [1] cannot do this.

To validate the capability of the proposed new 3D element, several well-established benchmark examples are examined. It is found that the element can simulate the size-dependent mechanical behaviors of structures very efficiently. Moreover, because the new C^0 low-order 8-node hexahedral element which has only three displacement DOFs and three rotation DOFs per node is directly derived from the virtual work principle, it is not only more concise in final formulation but also more efficient in computation at element level than the other existing 3D models.

2. Governing Equations of Modified Couple Stress Theory

Yang et al. [4] modified the original version of the couple stress theory [7, 8] by introducing an additional equilibrium condition to enforce the couple stress tensor to be symmetric. Consequently, there is no need to consider the antisymmetric terms of the curvatures in the deformation energy, and accordingly only one additional constant is required to represent the size-related material property.

In Yang's theory, the three displacement components can be written as

$$\mathbf{u} = \begin{Bmatrix} u \\ v \\ w \end{Bmatrix}, \tag{1}$$

whilst the strain $\boldsymbol{\varepsilon}$ and the physical rotation $\boldsymbol{\omega}$ are defined as the first-order derivatives of the displacements as follows:

$$\boldsymbol{\varepsilon} = \begin{Bmatrix} \varepsilon_{xx} \\ \varepsilon_{yy} \\ \varepsilon_{zz} \\ \gamma_{xy} \\ \gamma_{yz} \\ \gamma_{xz} \end{Bmatrix} = \begin{bmatrix} \partial/\partial x & 0 & 0 \\ 0 & \partial/\partial y & 0 \\ 0 & 0 & \partial/\partial z \\ \partial/\partial y & \partial/\partial x & 0 \\ 0 & \partial/\partial z & \partial/\partial y \\ \partial/\partial z & 0 & \partial/\partial x \end{bmatrix} \begin{Bmatrix} u \\ v \\ w \end{Bmatrix}, \tag{2}$$

$$\boldsymbol{\omega} = \begin{Bmatrix} \omega_x \\ \omega_y \\ \omega_z \end{Bmatrix} = \frac{1}{2} \begin{bmatrix} 0 & -\partial/\partial z & \partial/\partial y \\ \partial/\partial z & 0 & -\partial/\partial x \\ -\partial/\partial y & \partial/\partial x & 0 \end{bmatrix} \begin{Bmatrix} u \\ v \\ w \end{Bmatrix}. \tag{3}$$

Then, the curvature $\boldsymbol{\chi}$ can be derived from the physical rotation $\boldsymbol{\omega}$ by

$$\boldsymbol{\chi} = \begin{Bmatrix} \chi_{xx} \\ \chi_{yy} \\ \chi_{zz} \\ 2\chi_{xy} \\ 2\chi_{yz} \\ 2\chi_{xz} \end{Bmatrix} = \begin{bmatrix} \partial/\partial x & 0 & 0 \\ 0 & \partial/\partial y & 0 \\ 0 & 0 & \partial/\partial z \\ \partial/\partial y & \partial/\partial x & 0 \\ 0 & \partial/\partial z & \partial/\partial y \\ \partial/\partial z & 0 & \partial/\partial x \end{bmatrix} \begin{Bmatrix} \omega_x \\ \omega_y \\ \omega_z \end{Bmatrix}, \tag{4}$$

in which the coefficient "2" is employed to take the symmetry property of the curvatures into consideration in the deformation energy.

For isotropic linear elasticity problems, the stress $\boldsymbol{\sigma}$ can be obtained from the strain $\boldsymbol{\varepsilon}$ by using the constitutive equation:

$$\boldsymbol{\sigma} = \begin{Bmatrix} \sigma_{xx} \\ \sigma_{yy} \\ \sigma_{zz} \\ \sigma_{xy} \\ \sigma_{yz} \\ \sigma_{xz} \end{Bmatrix} = \mathbf{D}_n \boldsymbol{\varepsilon}\,, \tag{5}$$

with

$$\mathbf{D}_n = \frac{E}{(1+\nu)(1-2\nu)} \begin{bmatrix} 1-\nu & \nu & \nu & 0 & 0 & 0 \\ \nu & 1-\nu & \nu & 0 & 0 & 0 \\ \nu & \nu & 1-\nu & 0 & 0 & 0 \\ 0 & 0 & 0 & (1-2\nu)/2 & 0 & 0 \\ 0 & 0 & 0 & 0 & (1-2\nu)/2 & 0 \\ 0 & 0 & 0 & 0 & 0 & (1-2\nu)/2 \end{bmatrix}, \tag{6}$$

in which E and ν respectively are Young's modulus and Poisson's ratio. Meanwhile, the constitutive relationship between the couple stress $\mathbf{m}$ and the curvature $\boldsymbol{\chi}$ is given by

$$\mathbf{m} = \begin{Bmatrix} m_{xx} \\ m_{yy} \\ m_{zz} \\ m_{xy} \\ m_{yz} \\ m_{xz} \end{Bmatrix} = \mathbf{D}_c \boldsymbol{\chi}\,, \tag{7}$$

with

$$\mathbf{D}_c = \begin{bmatrix} 2\mu l^2 & 0 & 0 & 0 & 0 & 0 \\ 0 & 2\mu l^2 & 0 & 0 & 0 & 0 \\ 0 & 0 & 2\mu l^2 & 0 & 0 & 0 \\ 0 & 0 & 0 & \mu l^2 & 0 & 0 \\ 0 & 0 & 0 & 0 & \mu l^2 & 0 \\ 0 & 0 & 0 & 0 & 0 & \mu l^2 \end{bmatrix}, \tag{8}$$

in which l denotes the material length scale parameter and $\mu = E/2(1+\nu)$.

Besides, the stress and couple stress should satisfy the following equilibrium equations:

$$\sigma_{ik,i} - \frac{1}{2} e_{jlk} m_{ij,il} + f_k = 0\,, \tag{9}$$

in which e_{jlk} is the permutation symbol and f_k is the external body force load.

3. Finite Element Implementation

3.1. Variation principle

The derivation of the new 3D unsymmetric element starts with the virtual work principle. Let us consider a linear elastostatic body occupying the domain Ω with boundary Γ, the standard virtual work principle in the context of the modified couple stress theory can be expressed as

$$\int_\Omega \delta\bar{\boldsymbol{\varepsilon}}^{\mathrm{T}}(\bar{\mathbf{u}})\hat{\boldsymbol{\sigma}}\mathrm{d}\Omega+\int_\Omega \delta\bar{\boldsymbol{\chi}}^{\mathrm{T}}(\bar{\boldsymbol{\omega}})\hat{\mathbf{m}}\mathrm{d}\Omega-\int_\Omega \delta\bar{\mathbf{u}}^{\mathrm{T}}\mathbf{f}\mathrm{d}\Omega-\int_\Gamma \delta\bar{\mathbf{u}}^{\mathrm{T}}\mathbf{Q}\mathrm{d}\Gamma-\int_\Gamma \delta\bar{\boldsymbol{\omega}}^{\mathrm{T}}(\bar{\mathbf{u}})\mathbf{M}\mathrm{d}\Gamma=0\,, \quad (10)$$

in which $\bar{\boldsymbol{\varepsilon}}(\bar{\mathbf{u}})$ and $\bar{\boldsymbol{\omega}}(\bar{\mathbf{u}})$ respectively are the strain and physical rotation produced by the displacement test function $\bar{\mathbf{u}}$; $\bar{\boldsymbol{\chi}}(\bar{\boldsymbol{\omega}})$ is curvature further produced by the physical rotation $\bar{\boldsymbol{\omega}}(\bar{\mathbf{u}})$; $\hat{\boldsymbol{\sigma}}$ and $\hat{\mathbf{m}}$ denote the stress and couple stress trial functions; **f** and **Q** respectively are the external body force and boundary force, while **M** is the external boundary couple force. In the proposed element formulation, the above test functions and trial functions will be determined by using different interpolations, which is the main feature of the unsymmetric FEM [39-43].

Note that the curvatures which are the derivatives of the physical rotations are included in the virtual work principle. A standard FE implementation of Equation (10) will lead to the continuity requirements not only for the displacement test function $\bar{\mathbf{u}}$ but also for the physical rotation $\bar{\boldsymbol{\omega}}$, i.e., the C^1 continuity requirement, that may bring about great difficulties for developing a high-performance element with simple formulation, especially for the 3D hexahedral element models. To overcome this obstacle, the new element adopts an independently assumed rotation field $\bar{\boldsymbol{\theta}}$, which is directly derived from the nodal rotation DOFs, as the proper approximation of the true physical rotation $\bar{\boldsymbol{\omega}}(\bar{\mathbf{u}})$ from that the curvature test function is further deduced. Meanwhile, the penalty function is introduced into the virtual work principle to minimize the differences between these two rotation fields for enforcing the C^1 continuity condition in weak sense. Accordingly, Equation (10) is rewritten as

$$\int_\Omega \delta\bar{\boldsymbol{\varepsilon}}^{\mathrm{T}}(\bar{\mathbf{u}})\hat{\boldsymbol{\sigma}}\mathrm{d}\Omega+\int_\Omega \delta\bar{\boldsymbol{\chi}}^{\mathrm{T}}(\bar{\boldsymbol{\theta}})\hat{\mathbf{m}}\mathrm{d}\Omega-\int_\Omega \delta\bar{\mathbf{u}}^{\mathrm{T}}\mathbf{f}\mathrm{d}\Omega-\int_\Gamma \delta\bar{\mathbf{u}}^{\mathrm{T}}\mathbf{Q}\mathrm{d}\Gamma-\int_\Gamma \delta\bar{\boldsymbol{\theta}}^{\mathrm{T}}\mathbf{M}\mathrm{d}\Gamma+k\int_\Omega \delta\boldsymbol{\Lambda}^{\mathrm{T}}\boldsymbol{\Lambda}\mathrm{d}\Omega=0\,, \quad (11)$$

in which only the C^0 continuity is required for the displacement test function $\bar{\mathbf{u}}$; k is the penalty parameter and $\boldsymbol{\Lambda}$ is given by

$$\boldsymbol{\Lambda}=\bar{\boldsymbol{\omega}}(\bar{\mathbf{u}})-\bar{\boldsymbol{\theta}}\,. \quad (12)$$

More detailed discussions about the penalty item will be provided in Section 3.5.

3.2. The element's degrees of freedom

As shown in Figure 1, the new 8-node hexahedral element has three displacement DOFs and three rotation DOFs per node. The element nodal DOF vector $\mathbf{q}^e$ can be expressed as

$$\mathbf{q}^e = \left[\mathbf{q}_1^e \quad \mathbf{q}_2^e \quad \mathbf{q}_3^e \quad \mathbf{q}_4^e \quad \mathbf{q}_5^e \quad \mathbf{q}_6^e \quad \mathbf{q}_7^e \quad \mathbf{q}_8^e\right]^{\mathrm{T}}, \tag{13}$$

with

$$\mathbf{q}_i^e = \left[u_i \quad v_i \quad w_i \quad \theta_{xi} \quad \theta_{yi} \quad \theta_{zi}\right], \quad i = 1 \sim 8. \tag{14}$$

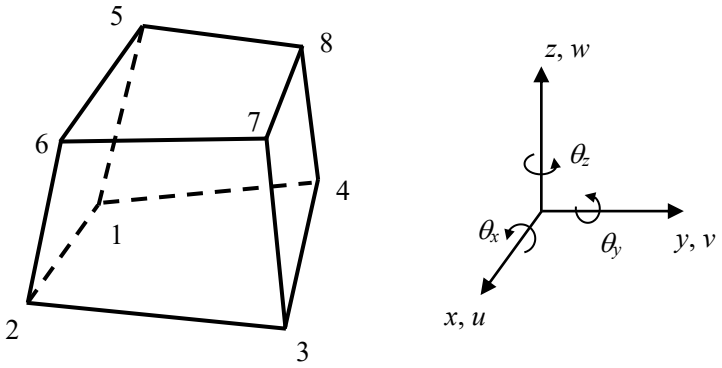

Figure 1. The 8-node hexahedral element with three rotation DOFs per node

3.3 The test functions

As discussed above, only the C^0 continuity is required for the displacement test function $\bar{\mathbf{u}}$ in Equation (11). The commonly used 3D isoparametric shape function may be the simplest choice. However, it can only provide poor performances in many cases, especially in bending-dominated problems. In the 2D formulation [1], the well-known Allman's interpolation is employed to determine the displacement test function. For the 3D cases, there are also some interpolations equipped with rotation DOFs. However, these interpolations seem somewhat complex. In this work, we formulate a more concise one by directly extending the 2D formulation proposed in [1] to the 3D case, as follows:

$$\bar{\mathbf{u}} = \begin{Bmatrix} \bar{u} \\ \bar{v} \\ \bar{w} \end{Bmatrix} = \bar{\mathbf{N}}\mathbf{q}^e, \quad \bar{\mathbf{N}} = \left[\bar{\mathbf{N}}_1 \quad \bar{\mathbf{N}}_2 \quad \ldots \quad \bar{\mathbf{N}}_8\right], \tag{15}$$

with

$$\bar{\mathbf{N}}_i = \begin{bmatrix} N_i & 0 & 0 & 0 & \frac{1}{2}N_i(z-z_i) & -\frac{1}{2}N_i(y-y_i) \\ 0 & N_i & 0 & -\frac{1}{2}N_i(z-z_i) & 0 & \frac{1}{2}N_i(x-x_i) \\ 0 & 0 & N_i & \frac{1}{2}N_i(y-y_i) & -\frac{1}{2}N_i(x-x_i) & 0 \end{bmatrix}, \quad i=1\sim 8, \tag{16}$$

in which (x, y, z) are the Cartesian coordinates and N_i is the standard 3D isoparametric shape function:

$$N_i = \frac{1}{8}(1+\xi_i\xi)(1+\eta_i\eta)(1+\zeta_i\zeta), \quad i=1\sim 8. \tag{17}$$

As shown in Equation (16), the displacements are effectively enriched by the nodal rotation DOFs by using the link interpolation technique. It can be easily proved that this displacement field can exactly ensure the C^0 continuity in any distorted geometry. Moreover, it coincides with the Allman's interpolation along the element boundaries.

Then, by substituting above the equations into Equation (2), the strain test function is obtained:

$$\bar{\boldsymbol{\varepsilon}} = \bar{\mathbf{B}}^n\mathbf{q}^e, \quad \bar{\mathbf{B}}^n = \begin{bmatrix} \bar{\mathbf{B}}_1^n & \bar{\mathbf{B}}_2^n & \dots & \bar{\mathbf{B}}_8^n \end{bmatrix}, \tag{18}$$

with

$$\bar{\mathbf{B}}_i^n = \begin{bmatrix} \bar{\mathbf{B}}_{\alpha i}^n & \bar{\mathbf{B}}_{\beta i}^n \end{bmatrix}, \quad i=1\sim 8, \tag{19}$$

in which

$$\bar{\mathbf{B}}_{\alpha i}^n = \begin{bmatrix} N_{i,x} & 0 & 0 \\ 0 & N_{i,y} & 0 \\ 0 & 0 & N_{i,z} \\ N_{i,y} & N_{i,x} & 0 \\ 0 & N_{i,z} & N_{i,y} \\ N_{i,z} & 0 & N_{i,x} \end{bmatrix}, \tag{20}$$

$$\bar{\mathbf{B}}_{\beta i}^n = \begin{bmatrix} 0 & \frac{1}{2}N_{i,x}(z-z_i) & -\frac{1}{2}N_{i,x}(y-y_i) \\ -\frac{1}{2}N_{i,y}(z-z_i) & 0 & \frac{1}{2}N_{i,y}(x-x_i) \\ \frac{1}{2}N_{i,z}(y-y_i) & -\frac{1}{2}N_{i,z}(x-x_i) & 0 \\ -\frac{1}{2}N_{i,x}(z-z_i) & \frac{1}{2}N_{i,y}(z-z_i) & \frac{1}{2}N_{i,x}(x-x_i)-\frac{1}{2}N_{i,y}(y-y_i) \\ \frac{1}{2}N_{i,y}(y-y_i)-\frac{1}{2}N_{i,z}(z-z_i) & -\frac{1}{2}N_{i,y}(x-x_i) & \frac{1}{2}N_{i,z}(x-x_i) \\ \frac{1}{2}N_{i,x}(y-y_i) & \frac{1}{2}N_{i,z}(z-z_i)-\frac{1}{2}N_{i,x}(x-x_i) & -\frac{1}{2}N_{i,z}(y-y_i) \end{bmatrix}. \tag{21}$$

(21)

From Equation (21), one can see that the strains are also effectively enhanced by the rotation DOFs.

As preceding discussed, the physical rotation test function in this work is approximated by the independently assumed rotation field $\bar{\boldsymbol{\theta}}$ which is interpolated by the nodal rotation DOFs:

$$\bar{\boldsymbol{\theta}} = \begin{Bmatrix} \bar{\theta}_x \\ \bar{\theta}_y \\ \bar{\theta}_z \end{Bmatrix} = \bar{\mathbf{N}}^{\theta}\mathbf{q}^{e}, \quad \bar{\mathbf{N}}^{\theta} = \begin{bmatrix} \bar{\mathbf{N}}_1^{\theta} & \bar{\mathbf{N}}_2^{\theta} & \ldots & \bar{\mathbf{N}}_8^{\theta} \end{bmatrix}, \tag{22}$$

with

$$\bar{\mathbf{N}}_i^{\theta} = \begin{bmatrix} 0 & 0 & 0 & N_i & 0 & 0 \\ 0 & 0 & 0 & 0 & N_i & 0 \\ 0 & 0 & 0 & 0 & 0 & N_i \end{bmatrix}, \quad i = 1 \sim 8. \tag{23}$$

Accordingly, the curvature test function can be easily obtained by

$$\bar{\boldsymbol{\chi}} = \bar{\mathbf{B}}^{c}\mathbf{q}^{e}, \quad \bar{\mathbf{B}}^{c} = \begin{bmatrix} \bar{\mathbf{B}}_1^{c} & \bar{\mathbf{B}}_2^{c} & \ldots & \bar{\mathbf{B}}_8^{c} \end{bmatrix}, \tag{24}$$

with

$$\bar{\mathbf{B}}_i^{c} = \begin{bmatrix} 0 & 0 & 0 & N_{i,x} & 0 & 0 \\ 0 & 0 & 0 & 0 & N_{i,y} & 0 \\ 0 & 0 & 0 & 0 & 0 & N_{i,z} \\ 0 & 0 & 0 & N_{i,y} & N_{i,x} & 0 \\ 0 & 0 & 0 & 0 & N_{i,z} & N_{i,y} \\ 0 & 0 & 0 & N_{i,z} & 0 & N_{i,x} \end{bmatrix}, \quad i = 1 \sim 8. \tag{25}$$

3.4 The trial functions

In the 2D element formulation [1], the stress trial function which conjugates with the strain test function is constructed at the base of the Airy stress solutions that can a prior satisfy all the related governing equations. However, the derivations of such analytical stress solutions in 3D elasticity are much more tedious than the 2D cases [43]. It will make the element construction procedure very cumbersome and thus is unpractical for developing a high-performance 3D element with concise expression. To circumvent this obstacle, we employ the equilibrium stress functions, which are derived by solving the equilibrium equations, instead of the analytical solutions to design the stress trial function. For simplicity, Table 1 directly lists twenty-one groups of such equilibrium stress functions while the derivation procedure is given in Appendix.

Then, the stress trial function $\hat{\boldsymbol{\sigma}}$ in Equation (11) can be firstly assumed as

$$\hat{\boldsymbol{\sigma}} = \mathbf{H}\boldsymbol{\alpha}, \tag{26}$$

with

$$\boldsymbol{\alpha} = \left[\alpha_1 \quad \alpha_2 \quad \alpha_3 \quad ... \quad \alpha_{21}\right]^{\mathrm{T}}, \tag{27}$$

$$\mathbf{H} = \left[\mathbf{H}_1 \quad \mathbf{H}_2 \quad ... \quad \mathbf{H}_{21}\right], \tag{28}$$

in which $\mathbf{H}_i$, (i=1~21) are given in Table 1.

Table 1. Twenty-one groups of stress functions used for the matrix **H** in Equation (28)

	i	1	2	3	4	5	6	7	8	9	10	11
$\mathbf{H}_i$	σ_{xx}^i	1	0	0	0	0	0	x	0	0	0	0
	σ_{yy}^i	0	1	0	0	0	0	0	x	0	0	0
	σ_{zz}^i	0	0	1	0	0	0	0	0	x	0	0
	σ_{xy}^i	0	0	0	1	0	0	0	0	0	x	0
	σ_{yz}^i	0	0	0	0	1	0	0	0	0	$-z$	x
	σ_{xz}^i	0	0	0	0	0	1	$-z$	0	0	0	0

	i	12	13	14	15	16	17	18	19	20	21
$\mathbf{H}_i$	σ_{xx}^i	0	y	0	0	0	0	0	z	0	0
	σ_{yy}^i	0	0	y	0	0	0	0	0	z	0
	σ_{zz}^i	$-z$	0	0	y	0	$-z$	0	0	0	0
	σ_{xy}^i	0	0	0	0	y	0	0	0	0	z
	σ_{yz}^i	0	0	$-z$	0	0	y	0	0	0	0
	σ_{xz}^i	x	0	0	0	$-z$	0	y	0	0	0

Next, to obtain the relationship between the element's DOFs and the above unknown coefficients,

the following condition based on the quasi-conforming theory [47], which belongs to the weighted residual method, is considered:

$$\int_{\Omega}\mathbf{H}^{\mathrm{T}}\left(\bar{\boldsymbol{\varepsilon}}-\mathbf{D}_{n}^{-1}\hat{\boldsymbol{\sigma}}\right)\mathrm{d}\Omega=\mathbf{0}, \tag{29}$$

in which $\bar{\boldsymbol{\varepsilon}}$ and $\mathbf{D}_n$ are respectively given by Equation (18) and Equation (6). Then, substitution of Equation (26) into Equation (29) yields

$$\boldsymbol{\alpha}=\mathbf{M}^{-1}\mathbf{V}\mathbf{q}^{e}, \tag{30}$$

where

$$\mathbf{M}=\int_{\Omega}\mathbf{H}^{\mathrm{T}}\mathbf{D}_{n}^{-1}\mathbf{H}\mathrm{d}\Omega, \tag{31}$$

$$\mathbf{V}=\int_{\Omega}\mathbf{H}^{\mathrm{T}}\bar{\mathbf{B}}^{n}\mathrm{d}\Omega. \tag{32}$$

Finally, by substituting Equation (30) back into Equation (26), we can obtain

$$\hat{\boldsymbol{\sigma}}=\hat{\mathbf{S}}^{n}\mathbf{q}^{e}, \tag{33}$$

with

$$\hat{\mathbf{S}}^{n}=\mathbf{H}\mathbf{M}^{-1}\mathbf{V}. \tag{34}$$

Besides, the couple stress trial function $\hat{\mathbf{m}}$, which is the conjugate pair of the curvature test function in energy form, is simply derived by substituting the curvature test function into the constitutive relationship given in Equation (7):

$$\hat{\mathbf{m}}=\mathbf{D}_{c}\bar{\mathbf{B}}^{c}\mathbf{q}^{e}=\hat{\mathbf{S}}^{c}\mathbf{q}^{e}. \tag{35}$$

3.5 The penalty function

As shown in Equation (11), the independently assumed rotation field $\bar{\boldsymbol{\theta}}$, that is interpolated by the element nodal rotation DOFs, is adopted as the proper approximation of the true physical rotation $\bar{\boldsymbol{\omega}}\left(\bar{\mathbf{u}}\right)$ which in nature is the derivatives of the displacement. The differences between these two fields can be expressed as

$$\boldsymbol{\Lambda}=\bar{\boldsymbol{\omega}}\left(\bar{\mathbf{u}}\right)-\bar{\boldsymbol{\theta}}=\bar{\mathbf{N}}^{\Lambda}\mathbf{q}^{e},\quad \bar{\mathbf{N}}^{\Lambda}=\left[\begin{array}{cccc}\bar{\mathbf{N}}_{1}^{\Lambda} & \bar{\mathbf{N}}_{2}^{\Lambda} & \ldots & \bar{\mathbf{N}}_{8}^{\Lambda}\end{array}\right]. \tag{36}$$

Making use of the equations given in Section 3.3, we can obtain

$$\bar{\mathbf{N}}_{i}^{\Lambda}=\left[\begin{array}{cc}\bar{\mathbf{N}}_{\alpha i}^{\Lambda} & \bar{\mathbf{N}}_{\beta i}^{\Lambda}\end{array}\right],\quad i=1\sim 8, \tag{37}$$

in which

$$\bar{\mathbf{N}}_{\alpha i}^{\Lambda}=\frac{1}{2}\begin{bmatrix}0 & -N_{i,z} & N_{i,y}\\ N_{i,z} & 0 & -N_{i,x}\\ -N_{i,y} & N_{i,x} & 0\end{bmatrix}, \tag{38}$$

$$\bar{\mathbf{N}}_{\beta i}^{\Lambda}=\frac{1}{4}\begin{bmatrix}N_{i,z}(z-z_i)+N_{i,y}(y-y_i)-2N_i & -N_{i,y}(x-x_i) & -N_{i,z}(x-x_i)\\ -N_{i,x}(y-y_i) & N_{i,z}(z-z_i)+N_{i,x}(x-x_i)-2N_i & -N_{i,z}(y-y_i)\\ -N_{i,x}(z-z_i) & -N_{i,y}(z-z_i) & N_{i,y}(y-y_i)+N_{i,x}(x-x_i)-2N_i\end{bmatrix}. \tag{39}$$

The penalty parameter *k*, which is proportional with the modulus according to the dimensional analysis, is used for the enforcement of the constraint $\mathbf{\Lambda}=\mathbf{0}$ and in general, the constraint will be satisfied more strictly as the penalty parameter *k* increases. In the previous work [1], the parametric study has been operated on the membrane element, and it is found that the convergence results can always be delivered when the ratio $k/\mu\geq 10^4$. In fact, the same conclusion are also obtained by operating the parametric study on the proposed new 3D hexahedral element. Therefore, this value can be properly adopted as the lower limit for the penalty parameter.

3.6 The stiffness matrix

Making use of the foregoing definitions, the final equations can be derived from Equation (11):

$$\mathbf{K}^e\mathbf{q}^e=\mathbf{P}^e, \tag{40}$$

in which $\mathbf{K}^e$ is the element stiffness matrix:

$$\mathbf{K}^e=\int_\Omega \bar{\mathbf{B}}^{n\mathrm{T}}\hat{\mathbf{S}}^n\mathrm{d}\Omega+\int_\Omega \bar{\mathbf{B}}^{c\mathrm{T}}\hat{\mathbf{S}}^c\mathrm{d}\Omega+k\int_\Omega \bar{\mathbf{N}}^{\Lambda\mathrm{T}}\bar{\mathbf{N}}^{\Lambda}\mathrm{d}\Omega, \tag{41}$$

and $\mathbf{P}^e$ is the equivalent load vector:

$$\mathbf{P}^e=\int_\Omega \bar{\mathbf{N}}^{\mathrm{T}}\mathbf{f}\mathrm{d}\Omega+\int_\Gamma \bar{\mathbf{N}}^{\mathrm{T}}\mathbf{Q}\mathrm{d}\Gamma+\int_\Gamma \bar{\mathbf{N}}^{\theta\mathrm{T}}\mathbf{M}\mathrm{d}\Gamma. \tag{42}$$

As discussed in [1, 22], severe locking behaviors may be observed when the full-integration scheme is used for the last penalty stiffness in Equation (41), because the two rotation fields shown in Equation (36) generally have different orders of interpolations. To overcome this possible locking problem, the one-point integral scheme suggested in [22] is employed for the penalty stiffness part here. However, it should be noted that, when the one-point integral is used, the constraint given by Equation (36) will no longer be exactly satisfied, especially when the element's shape is distorted.

4. Numerical Tests

The new C^0 8-node 48-DOF hexahedral element is applied to several numerical benchmarks to assess its capability for analyzing the size-dependent mechanical behaviors of materials. To the best of our knowledge, this is the first low-order C^0 3D element for the modified couple stress elasticity and no other element models of the same type are available. Thus, the results are only compared with the analytical solutions or overkill numerical solutions. In these tests, the penalty parameter is simply set as $k/\mu = 10^5$ in accordance with the discussions in Section 3.5.

4.1 The patch test

Figure 2 illustrates the model and typical meshes used for the patch test. The Mesh A contains seven distorted elements whilst the Mesh B and Mesh C respectively consist of 2×2×2 and 3×3×3 cuboid elements. The edge length of the cube is L=1mm. The material properties are defined as E=1.44Gpa, ν=0.25 and l=40μm.

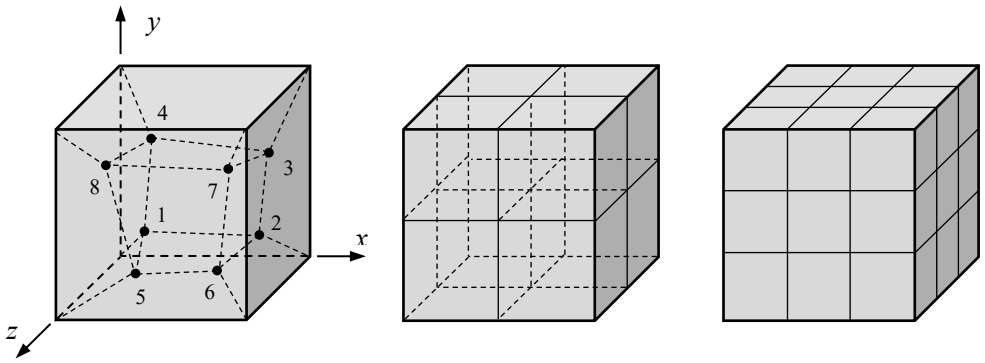

(a) Mesh A (b) Mesh B (c) Mesh C

Figure 2. The patch test

(a) The constant physical rotation case

To generate a constant physical rotation motion, the displacements and rotations at the outer nodes given by the following two equations are employed as the prescribed boundary conditions:

$$u = 1 + 4x + 7y + 10z, \quad v = 2 + 5x + 8y + 11z, \quad w = 3 + 6x + 9y + 12z\,. \tag{43}$$

$$\omega_x = -1, \quad \omega_y = 2, \quad \omega_z = -1\,. \tag{44}$$

Then, the values at the inner nodes are evaluated. The numerical results show that the constant physical rotation state can always be exactly reproduced.

(b) The constant couple stress case

To generate a constant couple stress state, the next quadratic displacement fields are considered:

$$u = x^2 + y^2 + z^2 - 5xy, \quad v = x^2 + y^2 + z^2 - 5yz, \quad w = x^2 + y^2 + z^2 - 5xz\,. \tag{45}$$

Correspondingly, the physical rotations are

$$\omega_x = -z + 3.5y, \quad \omega_y = -x + 3.5z, \quad \omega_z = -y + 3.5x\,. \tag{46}$$

The displacements and rotations at the boundary nodes calculated by using the above two equations are imposed to the cube as the boundary conditions, whilst the inner nodes are to be monitored. The numerical results show that the new element cannot reproduce the couple stress state when the badly distorted Mesh A is used. Note that the constant couple stress state in nature corresponds to a quadratic displacement motion, however, the new hexahedral element is only an 8-node low-order model. Even though the displacement interpolations have been enhanced by the independent nodal rotation DOFs, the quadratic parts of the displacements are still not complete. Moreover, as discussed in Section 3.6, the constraint given in Equation (12) will not be exactly satisfied because the reduced one-point integral strategy is employed for calculating the penalty stiffness to eliminate the possible locking problem. These are the main reasons why the new element fails in this test in distorted meshes.

Then, to validate the element's convergence property, the computations are repeated by simply subdividing the Mesh A. Note that the deduced meshes still consist of severely distorted elements. It can be seen from Table 2 that the errors can be effectively eliminated by the mesh refinement. Moreover, it is found that the new element can successfully pass this test by using the structured Mesh B and Mesh C. Considering that it is only a C^0 low-order 8-node model, the new element works reasonably well in this quadratic displacement test.

Table 2. The results of the constant couple stress case by subdividing the Mesh A

Node	(mm)	7 elements	56 elements	448 elements	Exact solutions
1	*u*	0.0042	-0.1564	-0.2136	-0.2100
	v	0.0065	-0.0800	-0.1168	-0.1125
	w	0.1409	0.0183	-0.0305	-0.0232

	u	-0.4503	-0.3662	-0.3311	-0.3413
2	*v*	0.8217	0.5263	0.4191	0.4334
	w	-0.4748	-0.3363	-0.3755	-0.3413
	u	-1.4194	-1.5191	-1.5201	-1.5454
3	*v*	0.3648	0.4007	0.3827	0.3594
	w	0.1179	0.0694	0.0982	0.0951
	u	-0.4165	-0.2995	-0.3433	-0.3338
4	*v*	-0.0976	-0.2081	-0.1520	-0.1726
	w	0.5702	0.4399	0.3470	0.3760
	u	0.4494	0.3377	0.2402	0.2528
5	*v*	-0.1912	-0.0428	-0.0385	-0.0476
	w	-0.4847	-0.5016	-0.4798	-0.4784
	u	-0.0709	-0.0642	-0.0331	-0.0146
6	*v*	-0.1909	0.0346	-0.0040	-0.0237
	w	-1.064	-1.3712	-1.3642	-1.2941
	u	-1.0484	-1.2161	-1.2129	-1.2145
7	*v*	-0.3633	-0.7166	-0.6977	-0.7155
	w	-0.9465	-1.0854	-1.0601	-1.0214
	u	0.3476	0.5198	0.4396	0.4604
8	*v*	-1.2228	-1.5510	-1.5200	-1.5399
	w	0.5311	0.4127	0.5048	0.4959

4.2 Torsion of a cylindrical bar

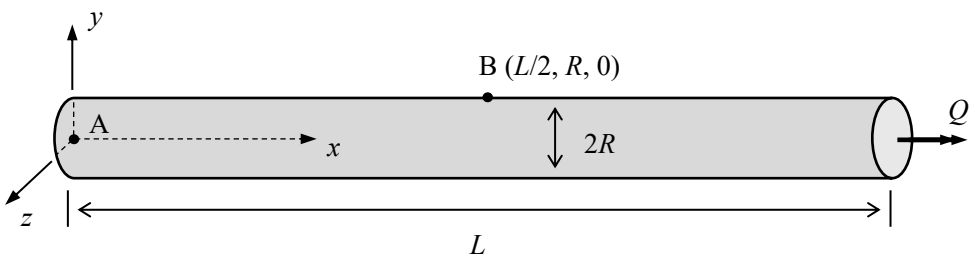

E=1.44GPa, ν=0.38, R=10μm, L=20R, Q=1 N · μm

Figure 3. Torsion of a slender cylindrical bar

As shown in Figure 3, the slender cylindrical bar is subjected to a torque Q at its right end. At the left end, the boundary conditions are set as

$$u = v = w = \omega_x = 0 \text{, at the surface } x = 0, \tag{47}$$

$$\omega_y = \omega_z = 0 \text{, at the point } x = 0,\ y = 0,\ z = 0. \tag{48}$$

In this test, the displacement w and physical rotation ω_x at the point B are monitored. The reference analytical solutions in the context of the modified couple stress theory are [4]:

$$w = \kappa x y,\ \omega_x = \kappa x, \tag{49}$$

in which κ is calculated by

$$Q_0 = \frac{1}{2}\pi\mu\kappa R^4,\quad Q = Q_0\left[1 + 6\left(\frac{l}{R}\right)^2\right]. \tag{50}$$

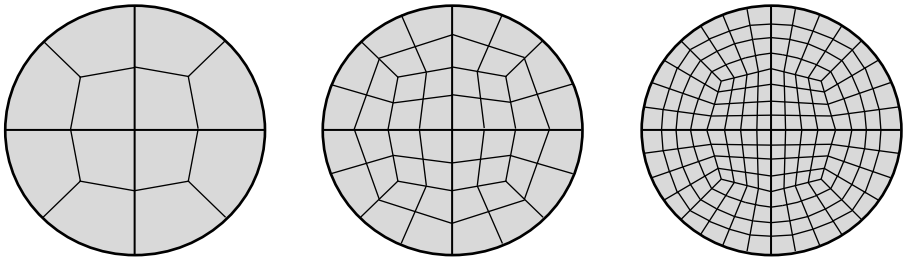

(a) 12×10 elements (b) 48×10 elements (c) 192×10 elements

Figure 4. The typical meshes for the cylindrical bar

First, the new element's convergence property is checked with the material length scale parameter l=17.6μm. The cylindrical bar is divided into ten segments along the longitudinal direction, while the typical section meshes are illustrated in Figure 4. Note that in the mesh 192×10, the elements have quite large aspect ratios. In Figure 5, the relative errors of the displacement and physical rotation are provided. One can observe that the new element converges well. Next, the influences of the length scale parameter are studied by using the mesh 192×10. As shown in Figure 6, good agreements are observed between the numerical results and the reference values, revealing that the element captures the size effect very effectively. Moreover, this test also shows that the new hexahedral element can still work well in slender geometries with high aspect ratios.

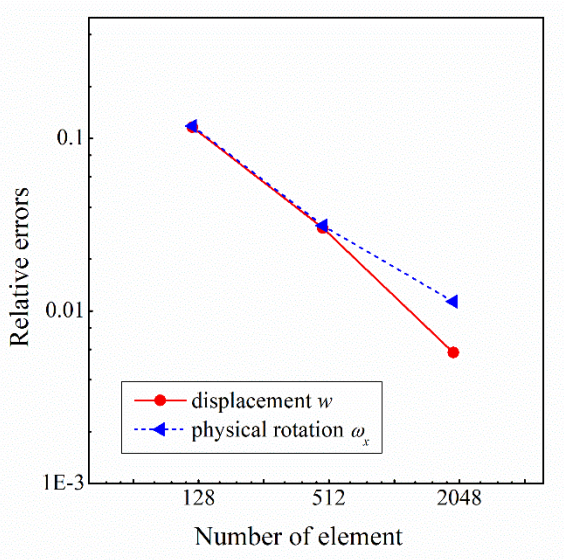

Figure 5. The relative errors of the displacement w and physical rotation ω_x at the point B of the cylindrical bar

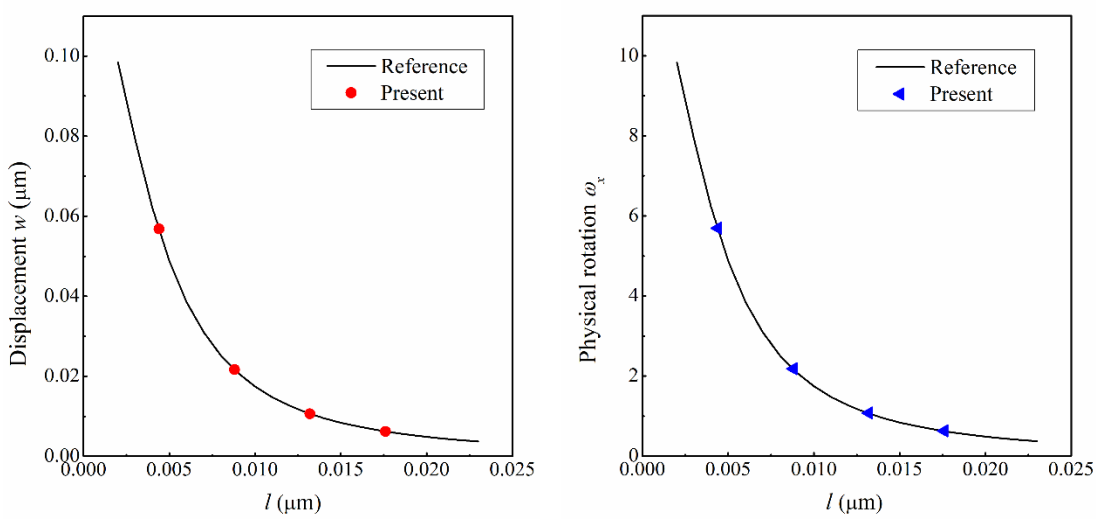

Figure 6. The displacement w and physical rotation ω_x at the point B versus the material length scale parameter calculated using 192×10 elements

4.3 The thin cantilever beam

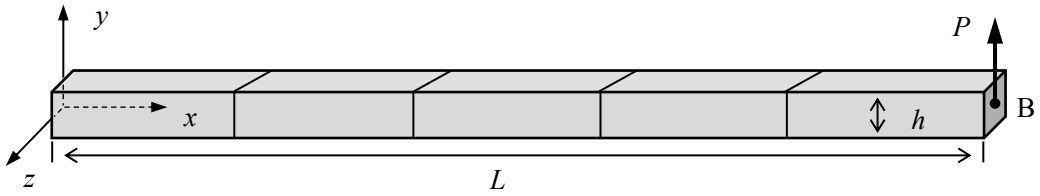

E=1.44GPa, ν=0.38, L=20h, P=100μN

Figure 7. The thin cantilever beam

As shown in Figure 7, the thin cantilever beam is subjected to a transverse load at its right tip. First, the case with beam height h=20μm and material length scale parameter l=17.6μm is considered and the beam is successively modeled by using 2×2×10, 4×4×20, 8×8×40 and 16×16×80 elements. The relative errors of the displacement w and physical rotation ω_z at the point B are provided in Figure 8. Since no analytical solutions are available for this problem, the results obtained by using 40000 elements are adopted as the reference values.

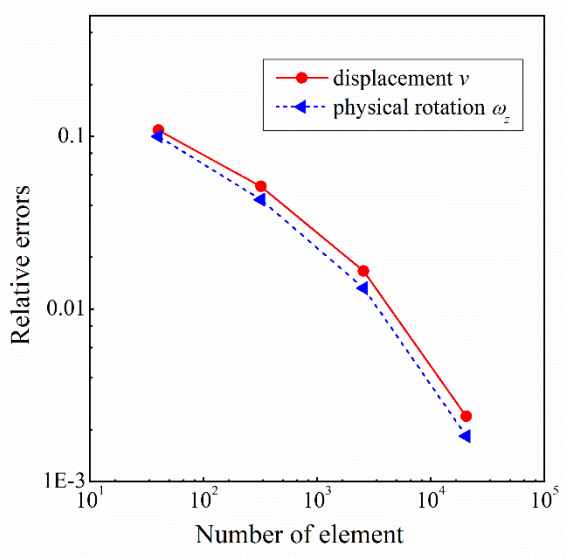

Figure 8. The relative errors of the displacement v and physical rotation ω_z at the point B of the cantilever beam with h=20μm and l=17.6μm

Second, the size effects are studied by evaluating the bending rigidities of the micro cantilever beam with different beam heights and material length scale parameters. The bending rigidity

calculated by the FE analysis is given by

$$D_{\mathrm{FEM}} = \frac{PL^3}{3v_{\max}bh^3}. \tag{51}$$

The numerical results obtained using the refined mesh 16×16×80 are summarized in Figure 9. It can be observed that, (i) for the beam with a fixed material length scale parameter, the bending rigidity will decrease as the beam height increases; (ii) for the beam with a fixed height, the bending rigidity will increase as the material length scale parameter increases.

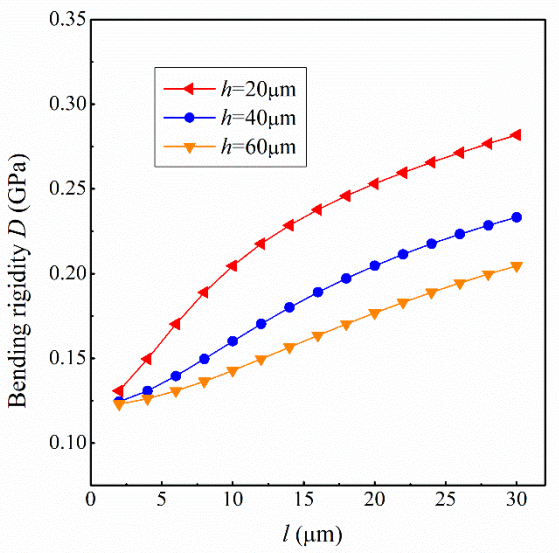

Figure 9. The bending rigidity of the cantilever beam with different h and l

4.4 The simple shear problem

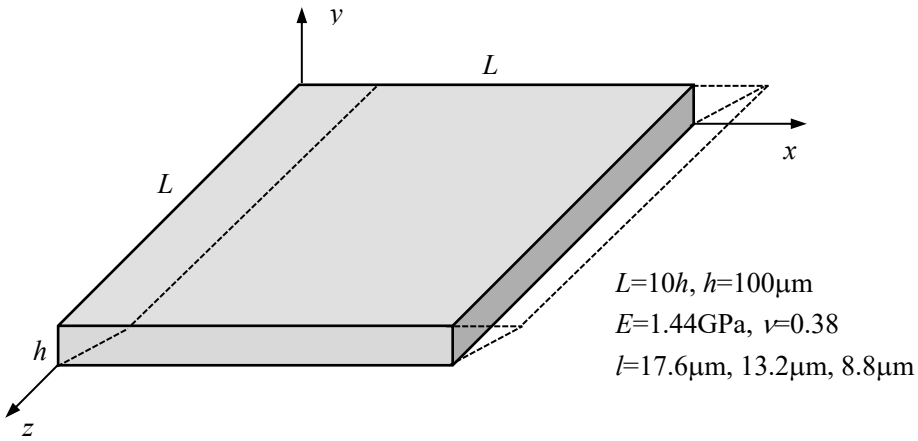

Figure 10. The simple shear problem

This test involves the classical simple shear problem proposed in [48]. As illustrated in Figure 10,

the block is clamped at the bottom surface, while the boundary condition at its top surface is set as

$$u = 1\,\mu\text{m} \quad \text{and} \quad v = w = \omega_x = \omega_y = \omega_z = 0\,. \tag{52}$$

The computations are operated by meshing the slender block into 40×40×10 elements. The variations of the displacement u and shear strain γ_{xy} along the path (x=0.5L, z=0.5L) are respectively plotted in Figure 11 and Figure 12, in which the analytical solutions are also provided for comparison. One can see that the numerical solutions are in good agreements with the reference values, demonstrating again that the new element simulates the size-dependent phenomenon well.

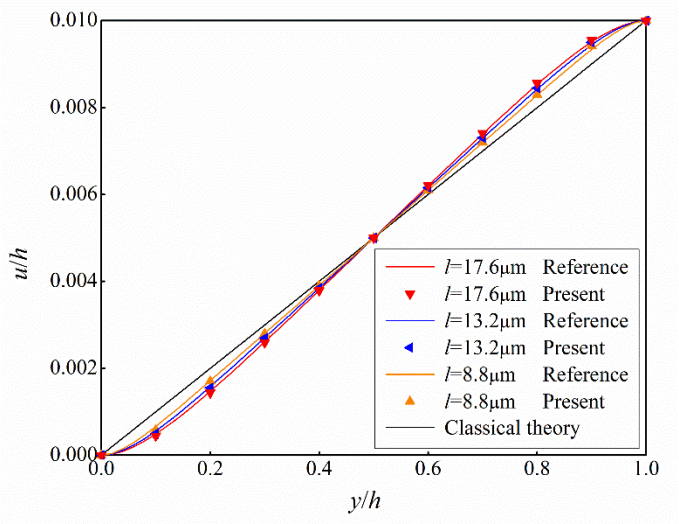

Figure 11. Distribution of displacement u along the path (x=0.5L, z=0.5L)

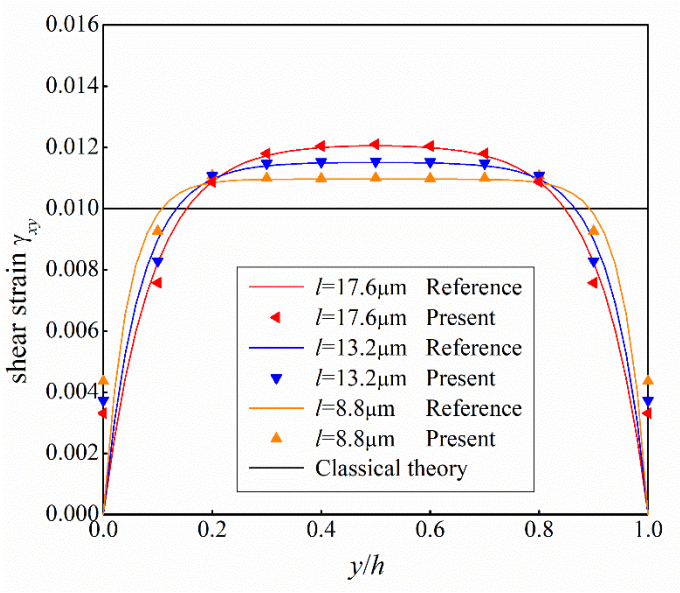

Figure 12. Distribution of shear strain γ_{xy} along the path (x=0.5L, z=0.5L)

4.5 The twist beam

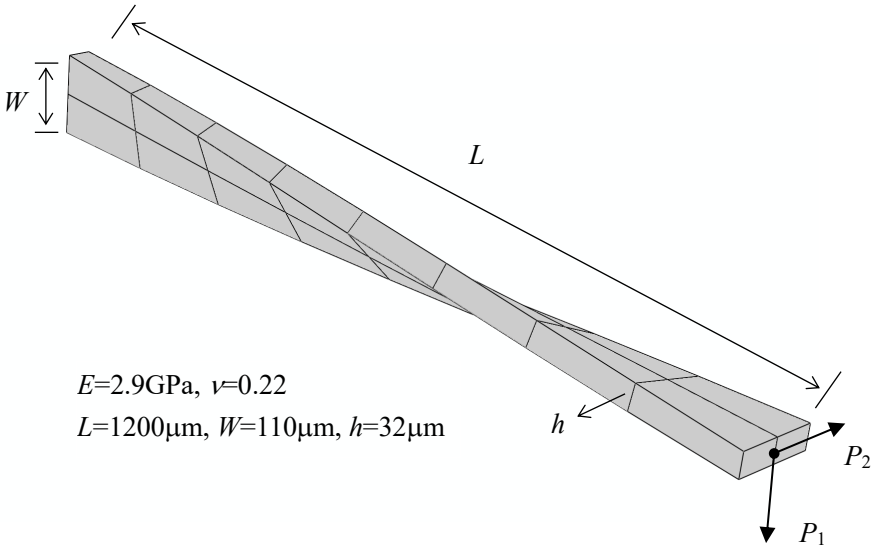

Figure 13. The twist beam and the typical mesh 8×2×1

The benchmark problem proposed in [41] is modified here to test the effects of warping on element performance. As shown in Figure 13, the 90° pre-twisted beam is clamped at the root and subjected to an in-plane or out-plane tip force. Four different material length scale parameters, including the special one l=0μm that corresponds to the classical elasticity, are considered. The tip deflections along the load direction are summarized in Table 3. One can clearly see that the new element can still provide satisfactory performance in warped geometry. Besides, this test also reveals that the new element can be easily used to efficiently solve the classical elasticity problems by simply setting the material length scale parameter as zero.

Table 3. The load-direction deflections of the twist beam (μm)

Mesh	8×2×1	16×4×2	32×8×4	64×16×8	Reference
Out-plane case: P_1=100μN, P_2=0					
l=17.6μm	11.062	11.137	11.266	11.315	11.323*
l=13.2μm	11.996	12.086	12.216	12.262	12.270*
l=8.8μm	13.587	13.667	13.776	13.817	13.825*
l=0μm	17.663	17.565	17.562	17.583	17.54**

in-plane case: P_1=0, P_2=100μN					
l=17.6μm	27.739	28.152	28.707	28.950	28.993*
l=13.2μm	32.034	32.540	32.998	33.182	33.214*
l=8.8μm	38.736	39.177	39.493	39.625	39.648*
l=0μm	54.548	54.105	54.083	54.161	54.24**

*The reference solutions are obtained using 16000 elements

**The reference solutions are provided in [41]

5. Conclusions

This paper proposes a simple but robust C^0 8-node hexahedral element with rotation DOFs for analysis of size-dependent problems in the context of the modified couple stress theory by extending the methodology developed in [1] to the 3D cases. In the present formulation, the key steps are to employ the independent nodal rotation DOFs to enrich the commonly used 3D isoparametric shape function for determining the displacement and strain test functions as well as to approximatively design the physical rotation field for deriving the curvature test function. The penalty function method is used for enforcing the C^1 continuity condition in weak sense. Besides, the stress trial function is formulated based on the equilibrium stress functions whilst the couple stress trial function is directly obtained from the curvature test function.

Five well-established benchmark tests are examined to validate the capability of the proposed 3D element. It is found that the new element can simulate the size-dependent mechanical behaviors of structures very effectively, exhibiting satisfactory numerical accuracy and good robustness to mesh distortion. In particular, it can still deliver good performances in high aspect ratio geometry and warping geometry. Besides, it is also shown that the new element can be easily used to solve the classical elastic problems in which the material length scale parameter is simply set as zero.

To the authors' best knowledge, it is the first C^0 low-order 3D element for the modified couple stress elasticity. Compared with the other existing 3D elements based on size-dependent continuum theories which are either C^1 models or higher-order C^0 models, the new element is not only more concise in construction procedure and final formulation but also more efficient in computation at element level, because it is directly derived from the virtual work principle and has only three displacement DOFs and three rotation DOFs per node. Moreover, the new element can be readily

extended to the geometric nonlinear analyses by using the incremental form proposed in [49].

Appendix

In this section, the derivations of the equilibrium stress functions listed in Table 1 are briefly introduced. When neglecting the couple stress and the body force load, the equilibrium equations shown in Equation (9) can be rewritten as

$$\begin{cases} \sigma_{xx,x} + \sigma_{xy,y} + \sigma_{xz,z} = 0 \\ \sigma_{xy,x} + \sigma_{yy,y} + \sigma_{yz,z} = 0 \\ \sigma_{xz,x} + \sigma_{yz,y} + \sigma_{zz,z} = 0 \end{cases}. \tag{A1}$$

To deduce the solutions of the above equations, the six stress components are firstly assumed as the following polynomials, in which twenty-four unknown coefficients are introduced:

$$\begin{cases} \sigma_{xx} = a_1 + a_2 x + a_3 y + a_4 z \\ \sigma_{yy} = b_1 + b_2 x + b_3 y + b_4 z \\ \sigma_{zz} = c_1 + c_2 x + c_3 y + c_4 z \\ \sigma_{xy} = d_1 + d_2 x + d_3 y + d_4 z \\ \sigma_{yz} = e_1 + e_2 x + e_3 y + e_4 z \\ \sigma_{xz} = f_1 + f_2 x + f_3 y + f_4 z \end{cases}. \tag{A2}$$

Then, by substituting Equation (A2) into Equation (A1), the coefficients c_4, e_4 and f_4 can be eliminated:

$$\begin{cases} a_2 + d_3 + f_4 = 0 \Rightarrow f_4 = -a_2 - d_3 \\ d_2 + b_3 + e_4 = 0 \Rightarrow e_4 = -d_2 - b_3 \\ f_2 + e_3 + c_4 = 0 \Rightarrow c_4 = -f_2 - e_3 \end{cases}, \tag{A3}$$

Subsequently, substitution of Equation (A3) back into Equation (A2) yields

$$\begin{cases} \sigma_{xx} = a_1 + a_2 x + a_3 y + a_4 z \\ \sigma_{yy} = b_1 + b_2 x + b_3 y + b_4 z \\ \sigma_{zz} = c_1 + c_2 x + c_3 y + \left(-f_2 - e_3\right) z \\ \sigma_{xy} = d_1 + d_2 x + d_3 y + d_4 z \\ \sigma_{yz} = e_1 + e_2 x + e_3 y + \left(-d_2 - b_3\right) z \\ \sigma_{xz} = f_1 + f_2 x + f_3 y + \left(-a_2 - d_3\right) z \end{cases}. \tag{A4}$$

Finally, by grouping the monomials shown in above Equation (A4) in accordance with the remained twenty-one coefficients, twenty-one groups of equilibrium stress functions which are summarized in Table 1 can be obtained.

Acknowledgements

The work is financially supported by the National Natural Science Foundation of China (Grant number 11702133) and the Natural Science Foundation of Jiangsu Province (Grant number BK20170772).

References

[1] Shang Y, Qian ZH, et al. A simple unsymmetric 4-node 12-DOF membrane element for the modified couple stress theory. International Journal for Numerical Methods in Engineering 2019; 119(9): 806-824.

[2] Altan BS, Aifantis EC. On some aspects in the special theory of gradient elasticity. Journal of the Mechanical Behavior of Materials 1997; 8(3): 231-282.

[3] Hadjesfandiari AR, Dargush GF. Couple stress theory for solids. International Journal of Solids and Structures 2011; 48(18): 2496-2510.

[4] Yang F, Chong ACM, et al. Couple stress based strain gradient theory for elasticity. International Journal of Solids and Structures 2002; 39(10): 2731-2743.

[5] Zozulya V. Higher order couple stress theory of plates and shells. ZAMM-Journal of Applied Mathematics and Mechanics/Zeitschrift für Angewandte Mathematik und Mechanik 2018; 98(10): 1834-1863.

[6] Thai HT, Vo TP, et al. A review of continuum mechanics models for size-dependent analysis of beams and plates. Composite Structures 2017; 177: 196-219.

[7] Toupin RA. Elastic materials with couple-stresses. Archive for Rational Mechanics and Analysis 1962; 11(1): 385-414.

[8] Mindlin RD, Tiersten HF. Effects of couple-stresses in linear elasticity. Archive for Rational Mechanics and Analysis 1962; 11(1): 415-448.

[9] Makvandi R, Reiher JC, et al. Isogeometric analysis of first and second strain gradient elasticity. Computational Mechanics 2018; 61(3): 351-363.

[10] Yu T, Zhang J, et al. A novel size-dependent quasi-3D isogeometric beam model for two-directional FG microbeams analysis. Composite Structures 2019; 211: 76-88.

[11] Thanh CL, Tran LV, et al. The size-dependent thermal bending and buckling analyses of composite laminate microplate based on new modified couple stress theory and isogeometric analysis. Computer Methods in Applied Mechanics and Engineering 2019; 350: 337-361.

[12] Liu S, Yu T, et al. Size and surface effects on mechanical behavior of thin nanoplates incorporating microstructures using isogeometric analysis. Computers & Structures 2019; 212: 173-187.

[13] Roque CMC, Fidalgo DS, et al. A study of a microstructure-dependent composite laminated Timoshenko beam using a modified couple stress theory and a meshless method. Composite Structures 2013; 96: 532-537.

[14] Askes H, Aifantis EC. Numerical modeling of size effects with gradient elasticity-formulation, meshless discretization and examples. International Journal of Fracture 2002; 117(4): 347-358.

[15] Zervos A, Papanastasiou P, et al. A finite element displacement formulation for gradient elastoplasticity. International Journal for Numerical Methods in Engineering 2001; 50(6): 1369-1388.

[16] Zervos A, Papanicolopulos SA, et al. Two finite-element discretizations for gradient elasticity. Journal of Engineering Mechanics 2009; 135(3): 203-213.

[17] Beheshti A. Finite element analysis of plane strain solids in strain-gradient elasticity. Acta Mechanica 2017; 228(10): 3543-3559.

[18] Papanicolopulos SA, Gulib F, et al. A novel efficient mixed formulation for strain-gradient models. International Journal for Numerical Methods in Engineering 2019; 117(8): 926-937.

[19] Choi JH, Lee BC. A three-node C^0 triangular element for the modified couple stress theory based on the smoothed finite element method. International Journal for Numerical Methods in Engineering 2018; 114(12): 1245-1261.

[20] Kwon YR, Lee BC. A mixed element based on Lagrange multiplier method for modified couple stress theory. Computational Mechanics 2017; 59(1): 1-12.

[21] Garg N, Han CS. Axisymmetric couple stress elasticity and its finite element formulation with penalty terms. Archive of Applied Mechanics 2015; 85(5): 587-600.

[22] Garg N, Han CS. A penalty finite element approach for couple stress elasticity. Computational Mechanics 2013; 52(3): 709-720.

[23] Wang CS, Zhang XK, et al. A 4-node quasi-conforming quadrilateral element for couple stress theory immune to distorted mesh. Computers & Structures 2016; 175: 52-64.

[24] Ma X, Chen WJ. Refined 18-DOF triangular hybrid stress element for couple stress theory. Finite Elements in Analysis and Design 2013; 75: 8-18.

[25] Zhao J, Chen WJ, et al. A refined nonconforming quadrilateral element for couple stress/strain gradient elasticity. International Journal for Numerical Methods in Engineering 2011; 85(3): 269-288.

[26] Phunpeng V, Baiz P. Mixed finite element formulations for strain-gradient elasticity problems using the FEniCS environment. Finite Elements in Analysis and Design 2015; 96: 23-40.

[27] Sze KY, Wu ZH. Twenty-four-DOF four-node quadrilateral elements for gradient elasticity. International Journal for Numerical Methods in Engineering 2019; 119(2): 128-149.

[28] Kahrobaiyan M, Asghari M, et al. A strain gradient Timoshenko beam element: application to MEMS. Acta Mechanica 2015; 226(2): 505-525.

[29] Kahrobaiyan M, Asghari M, et al. A Timoshenko beam element based on the modified couple stress theory. International Journal of Mechanical Sciences 2014; 79: 75-83.

[30] Ansari R, Shojaei MF, et al. A novel size-dependent microbeam element based on Mindlin's strain gradient theory. Engineering with Computers 2016; 32(1): 99-108.

[31] Reddy J, Romanoff J, et al. Nonlinear finite element analysis of functionally graded circular plates with modified couple stress theory. European Journal of Mechanics-A/Solids 2016; 56: 92-104.

[32] Ansari R, Shojaei MF, et al. Triangular Mindlin microplate element. Computer Methods in Applied Mechanics and Engineering 2015; 295: 56-76.

[33] Ansari R, Shojaei MF, et al. Nonlinear bending analysis of first-order shear deformable microscale plates using a strain gradient quadrilateral element. Journal of Computational and Nonlinear Dynamics 2016; 11(5): 051014.

[34] Papanicolopulos SA, Zervos A, et al. A three dimensional C^1 finite element for gradient elasticity. International Journal for Numerical Methods in Engineering 2009; 77(10): 1396-1415.

[35] Zervos A. Finite elements for elasticity with microstructure and gradient elasticity. International Journal for Numerical Methods in Engineering 2008; 73(4): 564-595.

[36] Torabi J, Ansari R, et al. Application of a non-conforming tetrahedral element in the context of the three-dimensional strain gradient elasticity. Computer Methods in Applied Mechanics and Engineering 2019; 344: 1124-1143.

[37] Zybell L, Mühlich U, et al. A three-dimensional finite element for gradient elasticity based on a mixed-type formulation. Computational materials science 2012; 52(1): 268-273.

[38] Kwon YR, Lee BC. Three dimensional elements with Lagrange multipliers for the modified couple stress theory. Computational Mechanics 2018; 62(1): 97-110.

[39] Shang Y, Ouyang WG. 4-node unsymmetric quadrilateral membrane element with drilling DOFs insensitive to severe mesh-distortion. International Journal for Numerical Methods in Engineering 2018; 113(10): 1589-1606.

[40] Huang J, Cen S, et al. An unsymmetric 8-node hexahedral solid-shell element with high distortion tolerance: Linear formulations. International Journal for Numerical Methods in Engineering 2018; 116(12-13): 759-783.

[41] Zhou PL, Cen S, et al. An unsymmetric 8-node hexahedral element with high distortion tolerance. International Journal for Numerical Methods in Engineering 2017; 109(8): 1130-1158.

[42] Shang Y, Cen S, et al. 8-node unsymmetric distortion-immune element based on Airy stress solutions for plane orthotropic problems. Acta Mechanica 2018; 229(12): 5031-5049.

[43] Xie Q, Sze K, et al. Modified and Trefftz unsymmetric finite element models. International Journal of Mechanics and Materials in Design 2016; 12(1): 53-70.

[44] Yunus SM, Pawlak TP, et al. Solid elements with rotational degrees of freedom: Part 1-hexahedron elements. International Journal for Numerical Methods in Engineering 1991; 31(3): 573-592.

[45] Sze KY, Soh AK, et al. Solid elements with rotational dofs by explicit hybrid stabilization. International Journal for Numerical Methods in Engineering 1996; 39(17): 2987-3005.

[46] Sze KY, Pan YS. Hybrid stress tetrahedral elements with Allman's rotational D.O.F.s. International Journal for Numerical Methods in Engineering 2000; 48: 1055-1070.

[47] Tang LM, Chen WJ, et al. Quasi-Conforming Elements for Finite Element Analysis. Journal of Dalian University of Technology 1980; 19(2): 17-35.

[48] Park SK, Gao XL. Variational formulation of a modified couple stress theory and its application to a simple shear problem. Zeitschrift Fur Angewandte Mathematik Und Physik 2008; 59(5): 904-917.

[49] Li Z, Cen S, et al. High-performance geometric nonlinear analysis with the unsymmetric 4-node, 8-DOF plane element US-ATFQ4. International Journal for Numerical Methods in Engineering 2018; 114(9): 931-954.